Electronic Supplementary Material (ESI) for Journal of Materials Chemistry C.

Supplementary Information
"Capturing excitonic and polaronic effects in lead iodide perovskites from many-body perturbation theory"

Pooja Basera*, Arunima Singh, Deepika Gill and Saswata Bhattacharya*
Department of Physics, Indian Institute of Technology Delhi, New Delhi 110016 India
*Corresponding author's email: Pooja.Basera@physics.iitd.ac.in [PB]
*saswata@physics.iitd.ac.in [SB]

Supporting Information

XVIII. Exciton lifetime using model BSE approach and its comparison with Wannier-Mott approach.

XIX. Direct-indirect nature of the bandgap (Rashba splitting)

XX. Effective dielectric constant

I. PBE functional convergence with high k-grid

We have shown convergence of the imaginary part of the dielectric function using PBE functional for $MAPbI_3$, $FAPbI_3$ and $CsPbI_3$, respectively. We have used DFPT method in order to show high k-grid sampling. We have observed that with increase in k-mesh, first peak does not change (shown by arrow) for all the systems ($MAPbI_3$, $FAPbI_3$ and $CsPbI_3$), unlike the case of mBSE calculations. In case of mBSE calculations, the first peak position has been slightly changed with an increase in k-mesh (see Fig 2(d)-(f) in main manuscript). This observation reinforces that, for PBE functional, convergence (in terms of bandgap) can be achieved at low k-grid sampling. However, for BSE calculations, we need to go at high k-grid sampling. Notably, the optical features or shape of spectra require high k-grid sampling in order to validate the results with experiment in case of both PBE and mBSE approach.

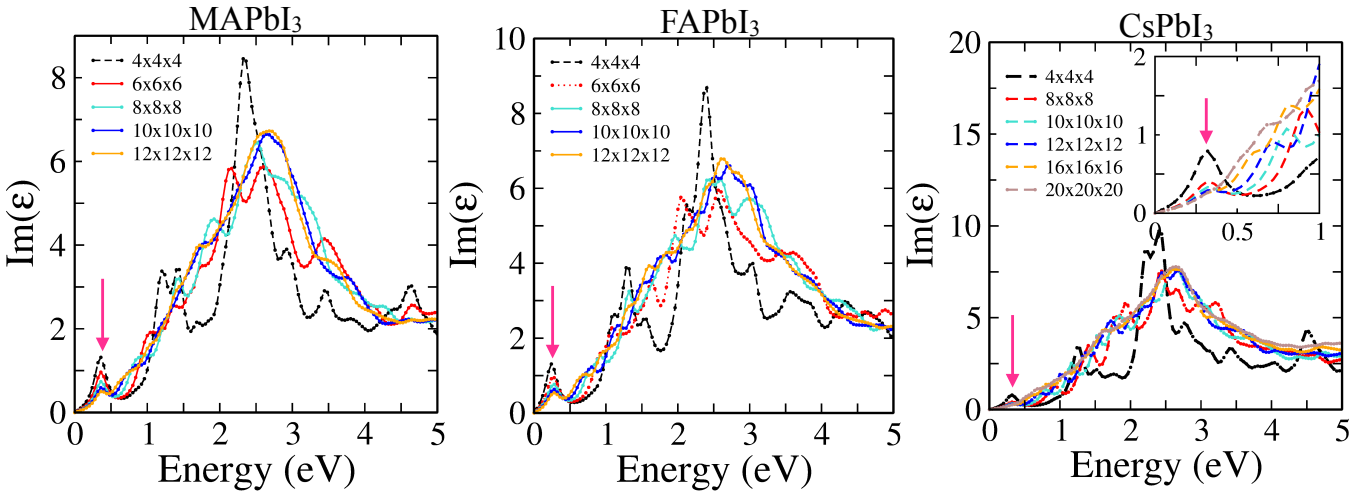

Figure S1: Variation of the imaginary part of dielectric function calculated using PBE functional with k-mesh.

II. Convergence of occupied and unoccupied bands in BSE calculations

For BSE calculations, the real and imaginary parts of the dielectric function are carefully examined with respect to a different number of occupied (NO) and unoccupied (NV) bands. The imaginary and real part of the dielectric function for different NO and NV [viz. NO = 4, NV = 8; NO = 20, NV = 20; NO = 22, NV = 22 etc.] are calculated for $FAPbI_3$ (see Fig S2). Fig S2(a) shows a slight change in the imaginary part of the dielectric function (only in the intensity of the peak), whereas it is clear from Fig S2(b) that there is significant change in the real part of the dielectric function. Here, we have observed that the static value of the real part of dielectric constant increases with an increase in NO, NV. The real and imaginary parts of the dielectric function are saturated at NO=NV=20. If we increase NO, NV beyond 20, no change in dielectric function is observed. Therefore, for rest of the calculations, we have set NO and NV at 20.

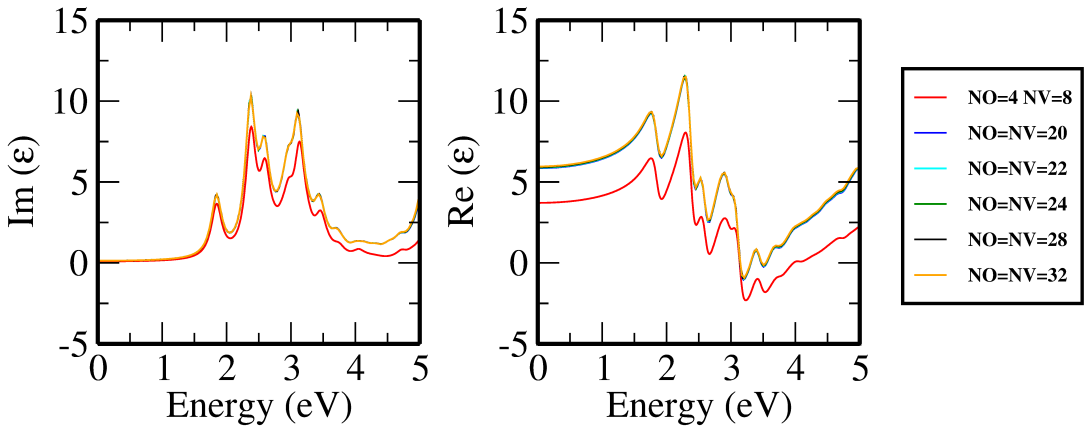

Figure S2: Convergence of number of bands in BSE calculations.

III. Effect of SOC on band structure

The bandgap calculated for $MAPbI_3$ from PBE and PBE+SOC are 1.54 eV and 0.49 eV, respectively. Here, we have observed that inclusion of SOC significantly reduces the bandgap by almost 1 eV. On comparing the band structure from PBE and PBE+SOC, we have discerned that, the valence and conduction band levels are significantly affected by SOC. The drastic changes mostly originate in the Pb-derived conduction band levels along with slight changes in the valence band levels.

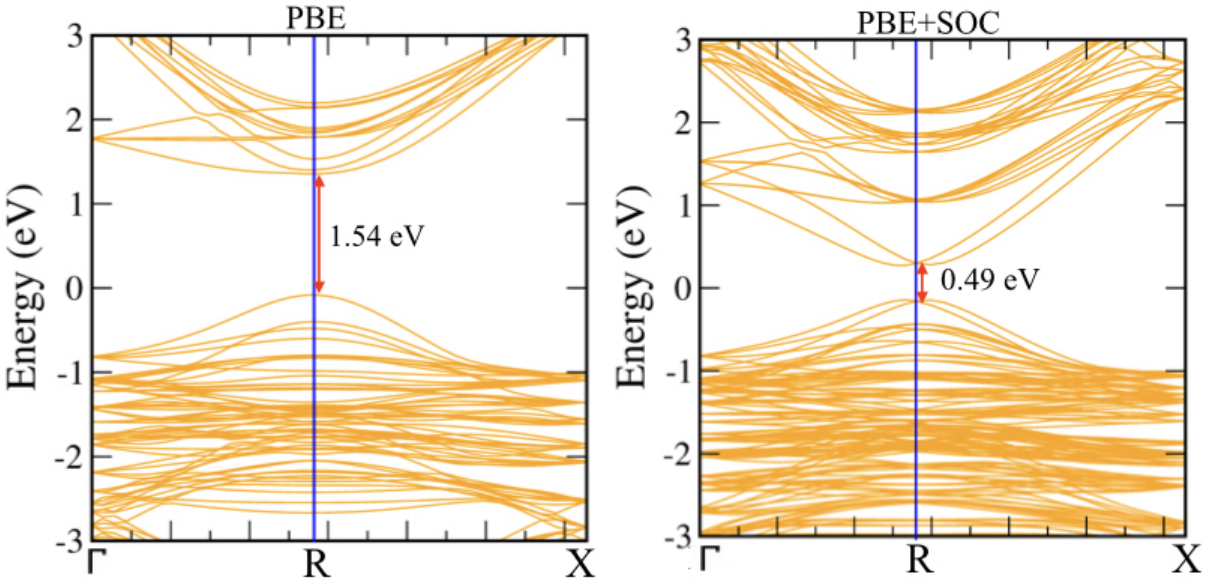

Figure S3: $MaPbI_3$ band structure, using PBE and PBE+SOC exchange correlation (ϵ_{xc}) functional

IV. Determination of GW bandgap for $MAPbI_3$, $FAPbI_3$ and $CsPbI_3$ perovskites

We have determined the optical response of $APbI_3$ perovskites by computing the imaginary part of dielectric function (Im (ε)). Initially, we have started with basic GGA (PBE) functional for the optical spectra of the cubic phase of $MAPbI_3$ perovskite, without incorporating SOC (see Fig1(a) in main manuscript). Subsequently, we have benchmarked the GW calculations with a comparative study of self-consistent GW (scGW) and single-shot GW (see Fig. S12). We have computed the optical spectra using scGW for $MAPbI_3$, and discern that scGW is four times more expensive as compared to single-shot GW, even for the calculations without SOC for a unitcell. Hence, we have performed all the following computations with single-shot GW. It is well known that single-shot GW calculation

is very much dependent on its starting point. Hence, it is crucial to obtain a pertinent starting point for the GW calculations. Therefore, from PBE calculation, we have obtained first peak at 1.55 eV, which is very close to the reported values (1.57–1.69 eV) [1–4].

Here, in our case, this matching is just the outcome of error cancellation due to self interaction error and non inclusion of SOC. Notably, this is not true for all the perovskites. We have shown in our recent work on $FAPbBr_3$, that the electron's self interaction error and SOC counter each other by unequal amount, thereby resulting in bandgap with PBE functional (1.72 eV) not in agreement with experimental value (2.23 eV) [5]. However, we have tried to further improve the optical peak of $MAPbI_3$, by performing GW@PBE calculations. This results in a large discrepancy in optical peak (2.37 eV) with respect to the reported value (see Fig1(a) in main manuscript). To correct it, we have explored BSE@GW calculation, which takes into account the e-h interactions. This leads to the reduction in the bandgap. Although BSE has reduced the GW bandgap, the achieved gap (2.12 eV) via BSE@GW@PBE is still far from the experimental value (see Fig1(a)). However, a sharp peak is observed for BSE calculations, which signifies the excitonic effect.

It is important to include the SOC effect in the $APbI_3$ perovskites, because of the presence of heavier elements like Pb and I. The role of SOC can be easily observed from the comparative analysis of band structures computed with and without SOC. The conduction band levels are significantly affected by SOC (Fig S3). Therefore, SOC should not be omitted in the calculations, even though PBE calculations yield the correct bandgap for $MAPbI_3$. The inclusion of SOC in PBE calculation tends to reduce the bandgap significantly by almost 1 eV. Here, we have observed a peak at 0.4 eV (see Fig 1b) in main manuscript). Then, we have performed GW@PBE+SOC calculations, hoping an improvement in the peak or bandgap, as it has a tendency to overestimate the bandgap. Unfortunately, GW@PBE+SOC calculation gives a peak value at 1.0 eV (see Fig1(b)). This value is in agreement with the previous theoretical calculations based on GW [1, 6], however still deviates from the experimental value. Note that, the value obtained from GW@PBE+SOC (1.0 eV) is still better, comparing the same with GW@PBE (2.37 eV). However, the BSE@GW@PBE+SOC gives the peak value at 0.72 eV which does not correlate well with the experimental value. Hence, we rationalize that, to perform single-shot GW on the top of PBE (with or without SOC) is not a good choice. Therefore, a theoretical approach is needed, which would better reproduce the experimental bandgap and peak position.

Hybrid functionals have emerged as an effective method, considering the agreement between theoretical calculations and experiments, at an affordable increase in the computational cost [7]. In HSE06 calculations, the exact exchange term from Hartree Fock (HF) is mixed with the semi-local ϵ_{xc} part of the DFT in a ratio (α). This ratio can be further adjusted in order to reproduce the experimental bandgap of the material. We have started with the default parameters of the HSE06 with a fraction of exact exchange of 25%, and screening parameter of 0.2 $Å^{-1}$. The peak position is obtained at 2.2 eV i.e far away from the experimental results. Hence, there is no use to perform GW@HSE06 and BSE@GW, because the peak value will be in any case overestimated due to poor starting point (see Fig 1(c) in main manuscript). Therefore, incorporation of SOC is important even for the hybrid functional HSE06. Initially, we have used standard parameter ($\alpha = 25\%$) of HSE06 with SOC, the peak position is obtained at 0.95 eV. Then, we have performed GW@HSE06+SOC with 25% α, that gives the first peak position at 1.37 eV. This peak position is closer to the experimental value, whereas, the subsequent BSE peak position at 1.11 eV deviates from the former (see Fig1(d)). Nevertheless, there is a possibility to further improve the peak position and the optical spectra. In view of this, we have increased the exact exchange parameter α and finally, the convergence is reached at $\alpha = 50\%$ for $MAPbI_3$. Hence, the optical peak or bandgap obtained using HSE06+SOC with $\alpha = 50\%$ is 1.55 eV [8, 9], which is in close agreement with the experiments (1.57 - 1.69 eV). Therefore, we conclude that HSE06+SOC (α=50%) is a prominent choice as a starting point for the GW in our calculations. GW@HSE06+SOC with (α= 50%) gives rise to a peak value at 1.67 eV (see Fig1(e))). On comparing Fig 1(a) and (e) in main manuscript, we can see that PBE and HSE06+SOC ($\alpha = 50$ %) tend to give the same value of the bandgap (1.55 eV), however, the first peak obtained from GW and BSE in both the cases are totally different.

The bandgap or first peak of optical spectra obtained from PBE for $FAPbI_3$ is 1.40 eV, which is very close to the experimental value 1.46 eV. However, GW@PBE and BSE@GW give the optical peak at 2.20 eV and 1.87 eV, respectively (see Fig S4(a)). Similarly, on the inclusion of SOC, the peaks are redshifted and the values are 0.25 eV, 0.96 eV and 0.65 eV corresponding to PBE+SOC, GW@PBE+SOC and BSE@GW, respectively (see Fig S4(b)). Likewise $MAPbI_3$, PBE+SOC is not appropriate to act as a starting point for GW calculations. We have shown in detail how all the peak positions (HSE06, GW@HSE06, BSE@GW) are shifted due to default value of α (25%) in HSE06 with and without SOC (see Fig S4(c) and (d)). In order to achieve an accurate peak position, tuning of the exact exchange parameter α by 53% works very well for $FAPbI_3$ perovskite. HSE06+SOC gives a peak position at 1.39 eV, whereas GW performed on the top of HSE06+SOC with α=53% provides a peak position at 1.45 eV (see Fig S4(e)). This value is in exact agreement with the experiments [10–12]. Therefore, this observation reinforces our

approach to accurately determine the fundamental gap (GW bandgap). Hence, we have generalized our approach for the HIOPs perovskite, now it will be interesting to discern its applicability for the inorganic perovskite.

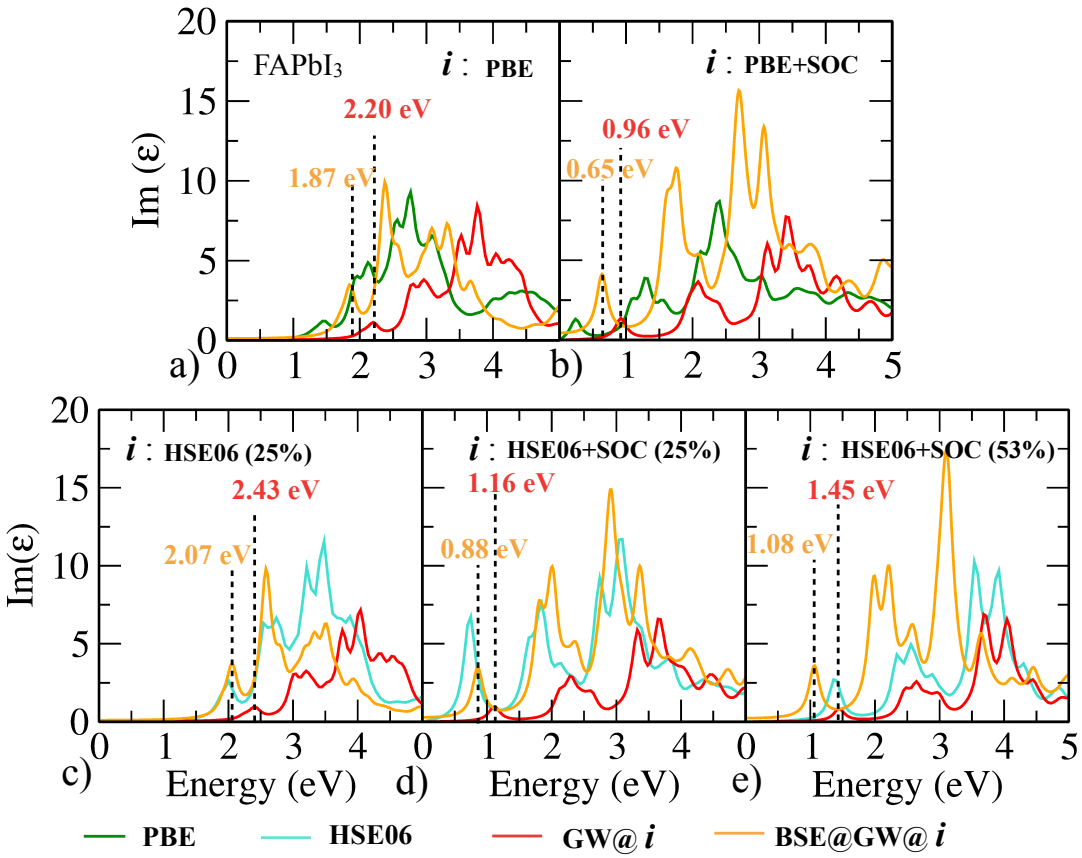

Figure S4: Imaginary part of dielectric function of $FAPbI_3$ calculated using single-shot GW and BSE, where several ϵ_{xc} functional are used as a starting point (i): (a) PBE (b) PBE+SOC (c) HSE06 (α= 25%) (d) HSE06+SOC (α= 25%) (e) HSE06+SOC (α= 53%).

For $CsPbI_3$ perovskite, we have obtained bandgap or optical peak at 1.50 eV using PBE functional. Unlike, HIOPs perovskites, there is no accidental matching of the PBE bandgap with the experimental value 1.73 eV [13, 14]. However, the bandgap can be overestimated using GW@PBE, but this results in peak value obtained at 2.07 eV, thus, not in agreement with the experiment (see Fig S5(a)). The BSE peak is obtained at 1.84 eV. Inclusion of SOC shifts the peak position at low energy value (see Fig S5(b)). The role of hybrid functional with and without SOC to be used as a starting point for the GW calculation can be seen explicitly in Fig S5(c) and (d), with default α= 25%. GW@HSE06 (α=25%) and GW@HSE06+SOC (α=25%) give peak position at 2.43 eV and 1.37 eV, respectively. These values are no longer close to the experimental data.

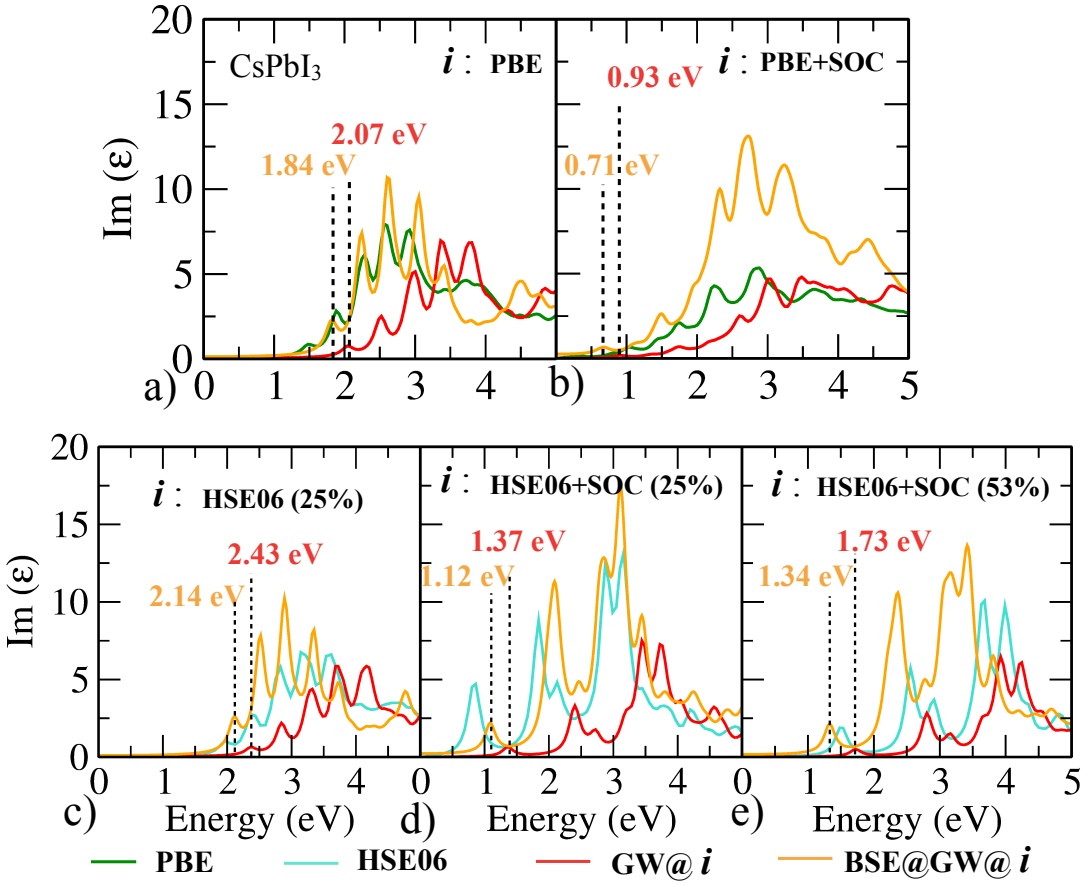

Figure S5: Optical spectra of $CsPbI_3$ calculated using single-shot GW and BSE, where several ϵ_{xc} functional are used as a starting point (i): (a) PBE (b) PBE+SOC (c) HSE06 (α= 25%) (d) HSE06+SOC (α= 25%) (e) HSE06+SOC (α= 53%).

Therefore, we have tuned α= 53% in HSE06+SOC calculations, that results in peak position at 1.69 eV. Then performing GW@HSE06+SOC (α=53%) leads to optical peak at 1.73 eV, which results in excellent agreement with the experiment (see Fig S5(e)) [13, 14]. Hence, we can conclude that, this method is sophisticated enough to predict accurate GW bandgap as well as correct optical peak position for all types of perovskites without going for computationally demanding high k-grid sampling.

V. Comparison between model-BSE (mBSE) and BSE approach

We have used a local model dielectric function $\varepsilon_{\infty}^{-1}$ in the BSE calculations, in order to converge the exciton binding energies on dense k-point grids. This model allows us to calculate the experimental features of the optical spectra. The parameter $\varepsilon_{\infty}^{-1}$ comes from DFPT calculations on a shifted high k-point grid (8×8×8 or 11×11×11). The screening length parameter (λ) are fitted to match the diagonal (G = G′) part of dielectric function from the GW calculations on the shifted 4 × 4 × 4 k-point grid. This approximation works very well, particularly, in the low energy part as shown in Fig S6 and S7. Here, we have shown for $MAPbI_3$, $FAPbI_3$ perovskite. The imaginary part of the dielectric function calculated with BSE@GW@PBE, including SOC, matches with the one, which is calculated with the model BSE (mBSE) method, where input is PBE+SOC. Therefore, the excitonic features (i.e first peak) information are always retained by mBSE approach. Note that both the calculations are carried out using a 4 × 4 × 4 k-point grid with a same starting point. It is worth to note that mBSE approach can predict the optical spectra for a dense high k-grid along with a very affordable computational cost. However, convergence of BSE calculations with such high k-grid is next to impossible, because of its huge computational cost.

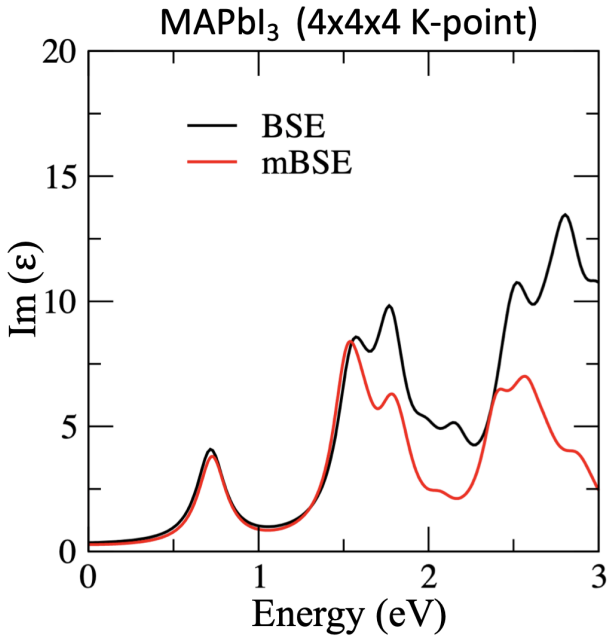

Figure S6: Imaginary part of dielectric function calculated using BSE and mBSE approach for $MAPbI_3$ perovskite.

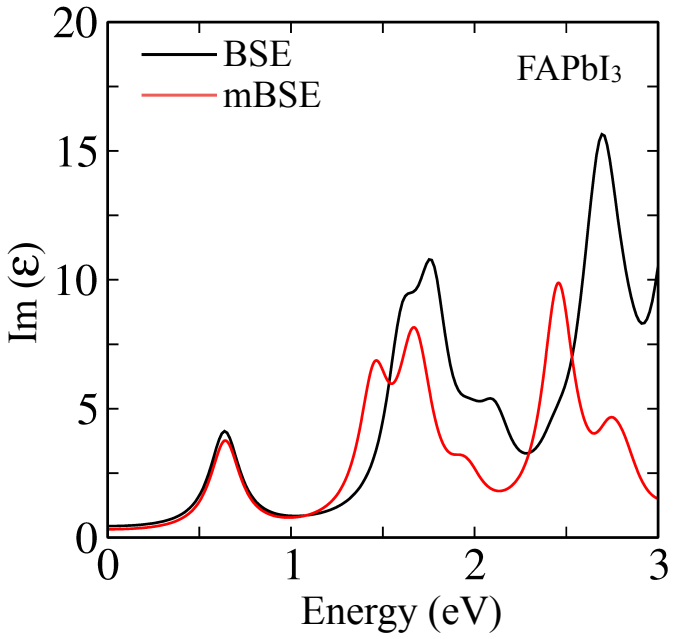

Figure S7: Imaginary part of dielectric function calculated using BSE and mBSE approach for $FAPbI_3$ perovskite.

VI. Projected density of states (PDOS) of $MAPbI_3$, $FAPbI_3$ and $CsPbI_3$

From Fig S8, we observe that valence band is primarily composed of I atom, whereas conduction band is mainly contributed by Pb atom for $MAPbI_3$, $FAPbI_3$ and $CsPbI_3$, respectively. Note that, the contribution of the organic cation (MA, FA) and the inorganic cation (Cs) is in deep inside the valence and conduction band. In short, cations do not play any role at the valence band and conduction band edges.

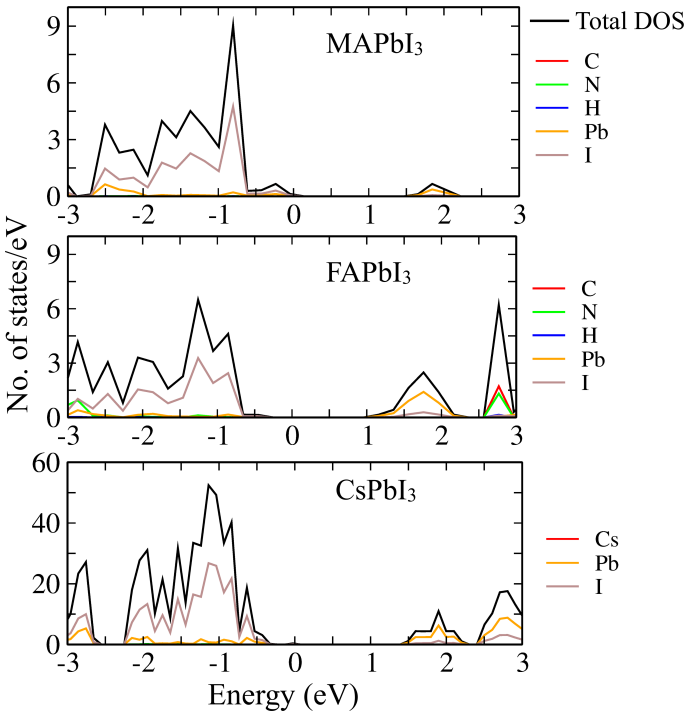

Figure S8: PDOS shows contribution of each atom.

VII. Previous reports on GW gaps, GW effective mass, BSE Im(ϵ) and the exciton binding energy

TABLE I: Previous reports on GW bandgap, GW effective mass and the exciton binding energy (E_B) of $APbI_3$ perovskites.

		Previous work	This work	Expt.
$MAPbI_3$	Bandgap (eV) GW@PBE+SOC	1.16/1.28 [1]	1.16	1.57–1.69 [1–4]
	Bandgap (eV) GW@HSE06+SOC	1.33 [15]	1.37	1.69 [1–4]
	Bandgap (eV) GW@HSE06+SOC (50%)	–	1.67	1.69 [1–4]
	Effective mass m*using GW	0.112 m_0 [16]	0.107 m_0	0.104±0.003 m_0 [17, 18]
	E_B (meV)	19[19], 45[20]	16.13	16 [18], 12±4 [21]
$FAPbI_3$	Bandgap (eV)	1.48 [20]	1.45	1.45[10], 1.48 [13], 1.43 [12]
	Effective mass m*using GW	0.101 m_0 [22]	0.102 m_0	0.095±10% m_0 [18]
	E_B (meV)	17[19], 35[20]	13.30	10-14 [18]
$CsPbI_3$	Bandgap (eV)	1.65 [23]	1.73	1.72 [21]
	Effective mass m*using GW	0.07 m_0, 0.18 m_0, 0.101 m_0 [22–24]	0.108	0.114±0.01 m_0 [18]
	E_B (meV)	24[19]	25.40, 14.60	15±1[18]

VIII. Variation of the exciton peak with respect to the K-point

The broadening parameter i.e SIGMA = 0.01 is same for all the $APbI_3$ perovskites (A = MA, FA and Cs). Still the features of excitonic peaks in Fig 5 (main manuscript) are different in all the three cases due to the excitonic effects. Yes, we agree with the reviewer's point that the width of the peak depends on the sampling of the Brillouin's zone (k-points). We have presented the comparison with different k-mesh viz. 4×4×4, 6×6×6 and 8×8×8 (see Fig S9). However, the trend for broadening remained same in every case , i.e. $CsPbI_3$ has broadened peak in comparison to that of $MAPbI_3$ and $FAPbI_3$, irrespective of the k-mesh size. It is well known that the width

determines the energy and the inverse life time of the excitons. The sharper the peak, longer the quasi particle lives and vice-versa. Therefore, qualitatively we can say that $CsPbI_3$ has the lowest exciton lifetime.

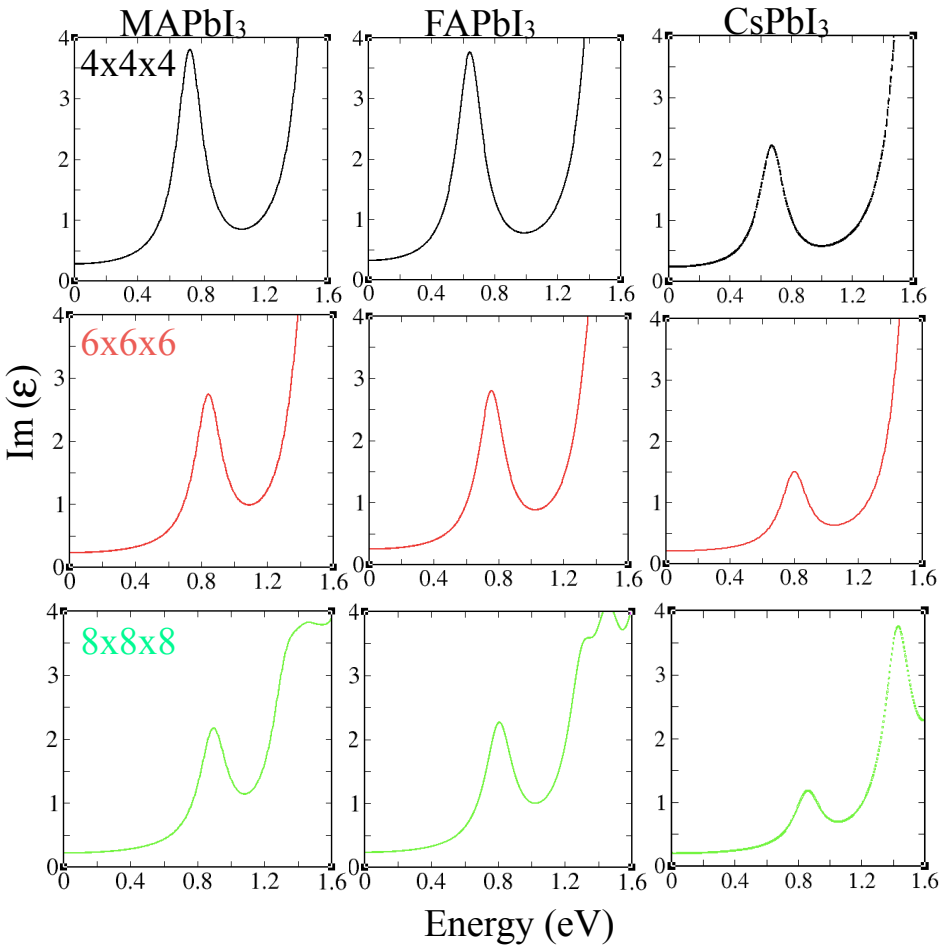

Figure S9: Qualitative analysis of exciton lifetime using mBSE exciton peak correponding to the K-point 4×4×4, 6×6×6 and 8×8×8

IX. Convergence criterion for the NBANDS and ENCUT

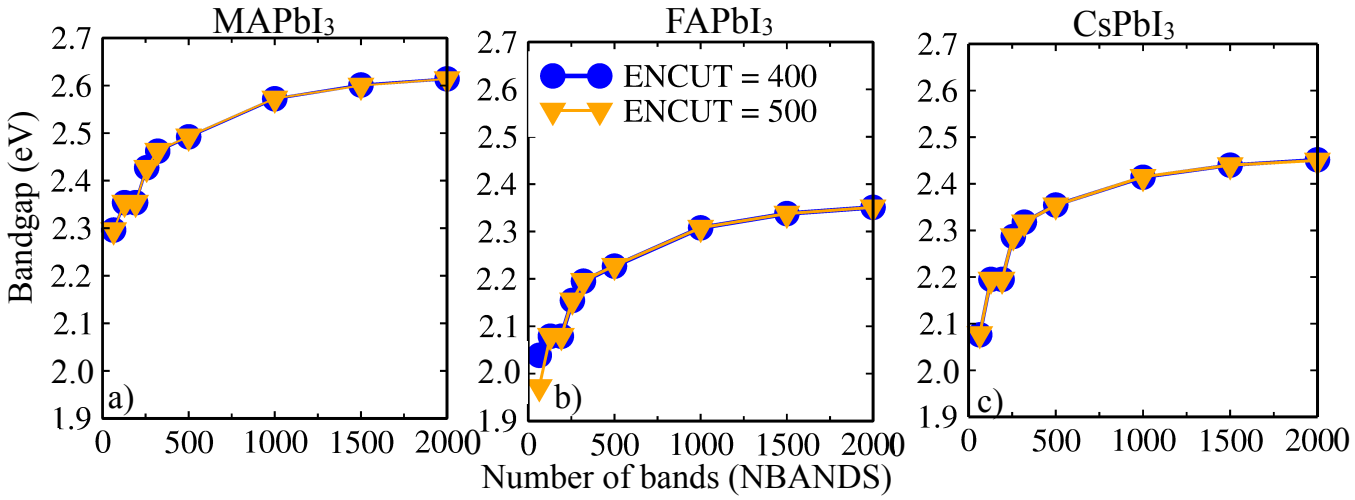

Figure S10: Convergence of the bandgap (eV) with respect to number of bands (NBANDS) and cutoff energy (ENCUT).

We have shown the convergence of the quasiparticle energies (and therefore of the quasiparticle bandgap) with respect to a set of number of bands (NBANDS), and the energy cutoff for the plane wave expansion (ENCUT). We have computed E_g as a function of NBANDS for fixed values of ENCUT. This scheme can leads to sufficiently well-converged results.

For our GW calculations, we have considered 1000 NBANDS and 400 ENCUT. Following this, the difference in bandgap using 2000 and 1000 NBANDS is around 0.02-0.04 eV. The difference is quite small, therefore we have considered 1000 bands in our calculations. However, for the convergence of energy cutoff i.e., ENCUT values, the difference between the bandgap using ENCUT 400, 500 eV is negligible. Note that, we have also checked the same for ENCUT= 600 eV and we do not observe any change in the value.

X. Effect of semicore electrons in the bandgap

The PAW pseodopotentials used in our calculations are Pb ($5d^{10}$ $6s^2$ $6p^2$ i.e. 14 valence electrons) and I ($5s^2$ $5p^5$ i.e. 7 valence electrons). However, we have also checked the influence of Pb ($6s^2$ $6p^2$ i.e. 4 valence electrons) in bandgap in our calculations.

For example, For $CsPbI_3$ with Pb (14 and 4 valence electrons) and I (7 valence electrons):
Bandgap ($5d^{10}$ $6s^2$ $6p^2$ i.e. 14 valence electrons) (PBE)= 1.49 eV
Bandgap ($6s^2$ $6p^2$ i.e. 4 valence electrons) (PBE)= 1.50 eV
Bandgap ($5d^{10}$ $6s^2$ $6p^2$ i.e. 14 valence electrons) (GW @PBE)= 2.04 eV
Bandgap ($6s^2$ $6p^2$ i.e. 4 valence electrons) (GW @PBE)= 2.17 eV

Similarly for $FAPbI_3$ with Pb (14 and 4 valence electrons) and I (7 valence electrons):
Bandgap ($5d^{10}$ $6s^2$ $6p^2$ i.e. 14 valence electrons) (PBE)= 1.31 eV eV
Bandgap ($6s^2$ $6p^2$ i.e. 4 valence electrons) (PBE)= 1.31 eV
Bandgap ($5d^{10}$ $6s^2$ $6p^2$ i.e. 14 valence electrons) (GW @PBE)= 1.93 eV
Bandgap ($6s^2$ $6p^2$ i.e. 4 valence electrons) (GW @PBE)= 2.04 eV

We observe that at PBE level, different pseudopotentials yield the same value of the bandgap. Notably, in order to check the influence of pseudopotentials, these calculations are done for ENCUT = 400 eV and NBANDS = 192. However, the convergence parameter required for the calculations is given in aforementioned section.

XI. Tuning of exact-exchange α parameter in hybrid calculations, followed by single-shot GW

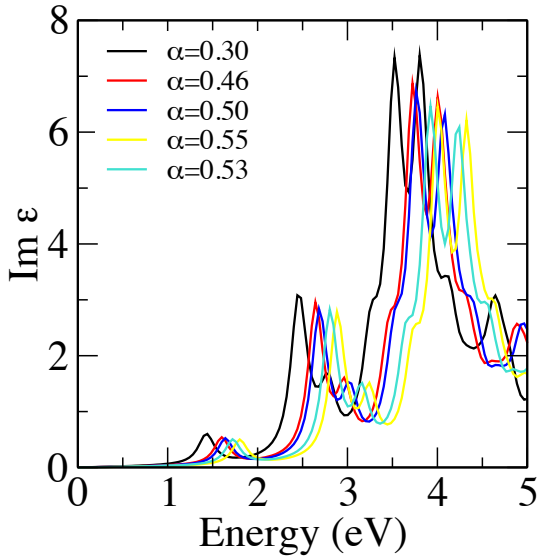

Figure S11: Variation in GW first peak in $CsPbI_3$ due to tuning of α parameter at starting HSE06+SOC point.

Note that, the GW and the BSE calculations will give the fundamental gap and the optical gap, respectively. In Figure S5, we have shown the GW optical spectra for $CsPbI_3$ perovskites. We obtain that the GW first peak shifts with the change in α parameter at starting HSE06+SOC point. We discern that with an increase in α parameter, the band gap also increases. The same procedure follows for $MAPbI_3$ and $FAPbI_3$ perovskites.

TABLE II: Variation of GW bandgap with respect to α.

α	GW bandgap of $CsPbI_3$
0.30	1.42
0.46	1.59
0.50	1.64
0.53	1.73
0.55	1.80

From Table III, we observe that the bandgap can be tuned with the variation in α parameter. For $\alpha = 0.53$, we have achieved the bandgap in agreement with the experimental values.

XII. Effective mass calculations for $MAPbI_3$

We have calculated the effective masses for both the splitted bands along R $\rightarrow$ X and R $\rightarrow$ Γ directions and take the average value of the effective masses.
For example: for $MAPbI_3$:

Hole effective masses:
m_h: -0.24 | band 44 | [0.50, 0.50, 0.50] $\rightarrow$ [0.00, 0.50, 0.00]
m_h: -0.20 | band 44 | [0.50, 0.50, 0.50] $\rightarrow$ [0.00, 0.00, 0.00]

Electron effective masses:
m_e: 0.257 | band 45 | [0.50, 0.50, 0.50] $\rightarrow$ [0.00, 0.50, 0.00]
m_e: 0.180 | band 45 | [0.50, 0.50, 0.50] $\rightarrow$ [0.00, 0.00, 0.00]
m_e: 0.236 | band 46 | [0.50, 0.50, 0.50] $\rightarrow$ [0.00, 0.50, 0.00]
m_e: 0.167 | band 46 | [0.50, 0.50, 0.50] $\rightarrow$ [0.00, 0.00, 0.00]
Hence, the average effective mass of electron (m_e) and hole (m_h) is 0.21 m_0 and 0.22 m_0, respectively.

XIII. Comparison between self-consistent GW (scGW) and single-shot GW for $MAPbI_3$

Self consistent GW (scGW) may be a viable choice, because for scGW, we don't need to test for the starting point, on the other hand single-shot GW is very much dependent on the starting point. Despite of that, in single-shot GW, the self-energy is calculated only once, therefore, it is computationally less expensive. However, self-consistent GW (scGW) is very much computationally expensive methods. We have computed optical spectra using scGW for $MAPbI_3$, and observe that scGW is four times more expensive as compared to single-shot GW, even for the calculations without SOC. The first peak observed for the single-shot GW and the scGW is 2.37 eV and 2.68 eV, respectively. For $MAPbI_3$, SOC tends to reduce the bandgap significantly by 1−1.2 eV. Hence, we can say that with the inclusion of SOC, scGW will give results very accurate as compared to single-shot GW. Nevertheless, to perform scGW is computationally very expensive method (at least four times that we have benchmarked) even for a small unitcell. That is why, in order to have a reliable results from single-shot GW, we should be very careful for the starting point. In view of this, we have tested our starting point very carefully via PBE, PBE+SOC, HSE06, HSE06+SOC (25%) and HSE06+SOC (50%). In single-shot GW, if we know the starting point accurately, then to perform single-shot GW is comparatively less expensive than scGW.

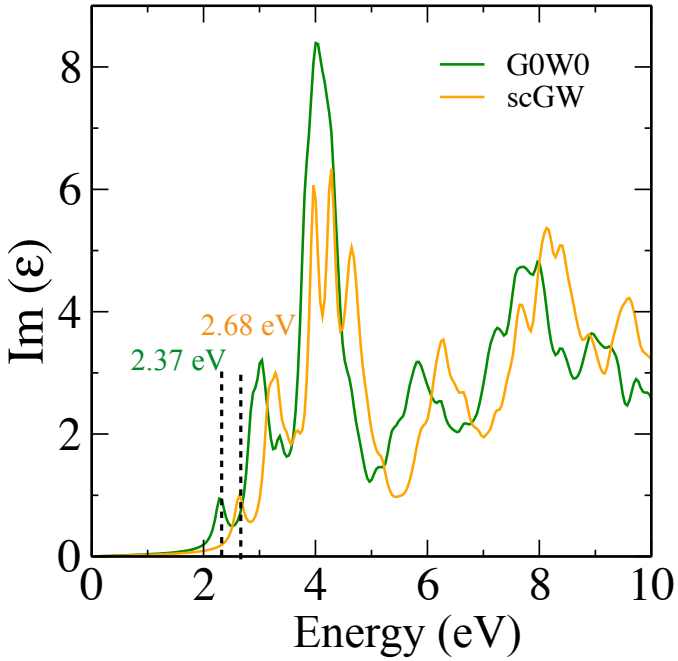

Figure S12: Optical spectra of $MAPbI_3$ using single-shot GW and self-consistent GW on the top of PBE without SOC.

XIV. Strength of electron-phonon coupling

The change in bond length, specific free volume, and atomic fluctuations would give a qualitative idea of coupling strength. Hence, on analyzing these parameters, we discern the strength of electron-phonon coupling in $APbI_3$ perovskites. For this purpose, we construct a 2×2×2 supercell using the optimized cubic phase unitcells of $MAPbI_3$, $FAPbI_3$ and $CsPbI_3$, containing 96 atoms in $MAPbI_3$ and $FAPbI_3$, and 40 atoms in the $CsPbI_3$, respectively. We have performed 10 ps long MD simulation run at 300 K with NVT ensemble (Nose-Hoover thermostat). The time step is taken as 1 fs. We have optimized the geometries of $MAPbI_3$, $FAPbI_3$, and $CsPbI_3$ at 0 K and and subsequently, the snapshots of the corresponding structures are taken from the MD simulation at 300 K. We have calculated the average bond length of Pb–I in the $MAPbI_3$, $FAPbI_3$ and $CsPbI_3$ systems at 0 K i.e., 3.21 Å, 3.24 Å, and 3.20 Å, respectively (see Table III).

TABLE III: Pb–I bond length (Å) of $APbI_3$ perovskites at 0 K and 300 K.

Temperature (K)	$MAPbI_3$	$FAPbI_3$	$CsPbI_3$
0	3.21	3.24	3.20
300	3.31	3.32	3.35

We observed that, at room temperature (300 K), the bond length increases to 3.31 Å, 3.32 Å, and 3.35 Å for $MAPbI_3$, $FAPbI_3$ and $CsPbI_3$, respectively. The increase in the Pb–I bond length in $CsPbI_3$ is larger than that of $MAPbI_3$ and $FAPbI_3$ (on reaching 300 K). This is because the larger A-site organic cations in $FAPbI_3$, suppress the deformation of the inorganic sublattice made of Pb and I. The observed change in the Pb–I bond length manifests the strong electron vibrational coupling in the $CsPbI_3$, followed by $MAPbI_3$ and $FAPbI_3$.
The aforementioned point can be further explained by the lattice free volume, which is defined as the difference between the unitcell volume and the constituent ions' volume. In general, a larger unoccupied volume yields more space for atomic motions, that tend to enhance the electron-phonon coupling. The volume of the optimized unitcell of $MAPbI_3$, $FAPbI_3$ and $CsPbI_3$ is calculated to be 260.92 $Å^3$, 262.56 $Å^3$ and 259.69 $Å^3$, respectively. Shannon ionic radii of MA^+, FA^+, Cs^+, Pb^{2+}, and I^- are 2.17 Å, 2.53 Å, 1.88 Å, 1.19 Åand 2.20Å, respectively. Each $APbI_3$ unitcell contains one A (MA^+, FA^+, Cs^+), one Pb^{2+}, and three I^-. Adding the spheres' volume in the unitcell yields the total ion volume of 183.57 $Å^3$, 208.59 $Å^3$ and 168.61 $Å^3$ for $MAPbI_3$, $FAPbI_3$, and $CsPbI_3$, respectively. The ratio between the unoccupied volume and the total volume is known as the specific free volume, which are obtained as 29.64%, 20.55% and 35.07%, for the $MAPbI_3$, $FAPbI_3$ and $CsPbI_3$, respectively (see Table IV). The smaller value of specific free volume infers the smaller amplitude of ion motions and hence, indicating the weaker electron-phonon coupling. Thus, it is anticipated that the electron-phonon coupling follows the sequence as $CsPbI_3$ > $MAPbI_3$ > $FAPbI_3$.

TABLE IV: Specific free volume for $APbI_3$ perovskites.

Specific free volume	$MAPbI_3$	$FAPbI_3$	$CsPbI_3$
in (%)	29.64	20.55	35.07

To corroborate our aforementioned results, we calculate the canonically averaged root mean square deviation of the position of each atom i, denoted by σ_i.

$$\sigma_i = \sqrt{\left\langle \left(\vec{r}_i - \vec{r}_i'\right)^2 \right\rangle} \tag{1}$$

where $\vec{r}_i$ and $\vec{r}_i'$ represent the location of atom i at time t along the 10 ps long MD trajectory at 300 K and initial optimized structure at 0 K. A smaller value of averaged root mean square deviation (σ_i) indicates the weaker electron-phonon coupling and the smaller atomic vibration fluctuation in the system. We have calculated the averaged root mean square deviation (σ_i) only for the positions of Pb and I atoms in $APbI_3$ perovskites, because the highest occupied molecular orbitals (HOMO) and lowest unoccupied molecular orbitals (LUMO) primarily consist of Pb and I orbitals (Figure S8). From Table V, the σ_i has the following trend for the positions of I and Pb atoms: $CsPbI_3$ > $MAPbI_3$ > $FAPbI_3$.

TABLE V: Averaged root mean square deviation in $APbI_3$ perovskites.

σ_i	$MAPbI_3$	$FAPbI_3$	$CsPbI_3$
Pb	0.295	0.135	0.306
I	0.516	0.347	0.679

The trend observed in case of atomic fluctuations reflect the same for electron-phonon couplings as well. Thus, the detailed analysis of bond length, specific free volume, and atomic fluctuation are in agreement with each other and

corroborate the fact that electron-phonon coupling is strongest in the $CsPbI_3$, with significant reduction in $MAPbI_3$ and $FAPbI_3$. Therefore, the effect of electron-phonon coupling tends to broaden the peak of $CsPbI_3$ significantly as compared to $MAPbI_3$ and $FAPbI_3$. Therefore, it validates the conclusion of Fig 7 in main manuscript, that exciton lifetime will follow the sequence as $FAPbI_3 > MAPbI_3 > CsPbI_3$.

XV. DFT-$\frac{1}{2}$ method for determining bandgap in $APbI_3$ perovskites

We have performed our calculation with DFT-$\frac{1}{2}$ method. The DFT-$\frac{1}{2}$ method attempts to correct the DFT self-interaction error by defining an atomic self-energy potential that cancels the electron-hole self-interaction energy. The DFT-$\frac{1}{2}$ method stems from Slater's proposal of an approximation for the excitation energy, a transition state method, to reduce the band gap inaccuracy by introducing a half-electron/half-hole occupation. Ferreira et al. [25] extended the method to modern DFT and particularly to solid-state systems, by assuming that the excited electron in the conduction band of a semiconductor usually occupies Bloch-like states with nearly vanishing self-energy, while the hole left in the valence band is localized with a finite self-energy. The self-energy of the hole was corrected by modifying the corresponding pseudopotentials of the atoms (in real space) by removing half an electron from the orbitals that contribute to the top of the valence band. Therefore, this method is capable enough to predict bandgap close to experiment with the same computational cost as standard DFT, however, this method imposes correction only to the valence band. Hence, conduction band level information is not predicted with the same accuracy as of valence band. Notably for DFT-$\frac{1}{2}$, we have imposed correction only on Pb and I atom pseudopotentials, because rest of the atoms will not contribute at the band edges. From the computational perspective, this method is really very useful to predict at least the correct valence band edge position. Still, we beleive that the starting point approach which we have used in our calculation is more effective to determine the valence band as well as conduction band edge positions along with the bandgap.

TABLE VI: Bandgap computed using DFT-$\frac{1}{2}$ +SOC method.

$APbX_3$	Bandgap (eV) (DFT-$\frac{1}{2}$+SOC)	Experimental bandgap (eV)
$MAPbI_3$	1.45	1.50 - 1.69
$FAPbI_3$	1.36	1.40 - 1.48
$CsPbI_3$	1.50	1.72

XVI. PBE+U method for determining bandgap in $APbI_3$ perovskites

We have performed the PBE+U calculation as a starting point for GW and BSE. We have chosen Hubbard parameter U = 2.3 eV, 2.3 eV and 6 eV for $MAPbI_3$, $FAPbI_3$ and $CsPbI_3$, respectively.

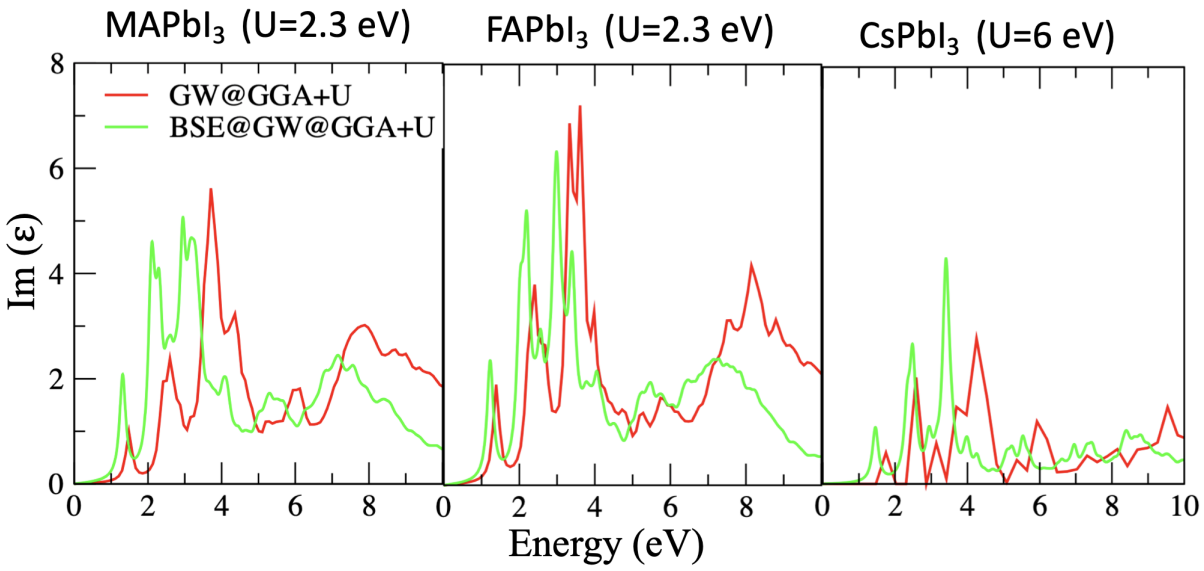

Figure S13: Optical spectra computed with PBE+U as a starting point for $MAPbI_3$, $FAPbI_3$ and $CsPbI_3$, respectively.

We obtain the following GW bandgap:
GW@PBE+U method can predict the bandgap accurately by tuning the Hubbard U parameter. In GGA+U

TABLE VII: GW bandgap computed using PBE+U method (including SOC).

$APbX_3$	Bandgap (eV) (GW@PBE+U)
$MAPbI_3$	1.50
$FAPbI_3$	1.40
$CsPbI_3$	1.83

method, still we are not able to define the correct band edge positions (VBM and CBm), that may impact the formation energy of charged system (see details in our previous work [5, 8], where we have shown how the valence band edge position influences the thermodynamic stability.
However, in the literature, this work [26], has shown the effect of starting point and self-consistency within GW on the band edge positions of semiconductors and insulators. They have found that, compared to calculations based on a semi-local starting point, the use of a hybrid-functional starting point shows a larger quasiparticle correction for both band edge states. That's why we have used the approach that can predict the bandgap as well as band edge position correctly.

XVII. Fat band structure of $APbI_3$ perovskites

We have computed fat band structure for $APbI_3$ perovskite. The fat band structure helps to compute the exciton radius from the model BSE calculations.

TABLE VIII: Comparison of exciton radius from Wannier-Mott approach and model-BSE approach.

Exciton radius of $APbX_3$	Wannier-mott (nm)	model-BSE (nm)
$MAPbI_3$	4.69	4.9
$FAPbI_3$	5.30	6.0
$CsPbI_3$	3.72	3.9

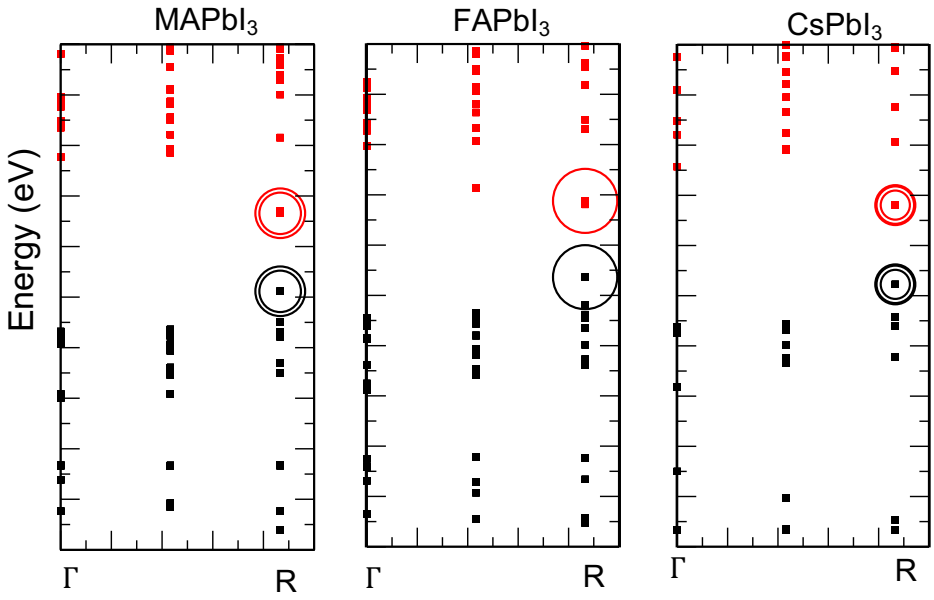

Figure S14: Fat band picture of excitons in $APbX_3$ perovskites. The black and red dots correspond to hole and electron eigenvalues along the high symmetry path Γ→ R. The radii of the circles represent the contribution of the e-h pair at the R-point to the first exciton wave function.

XVIII. Exciton lifetime using model BSE approach and its comparison with Wannier Mott approach

We have used the approach presented by Spataru et al. [27] and the same approach has been used in [28]. By using the same approach, we have calculated radiative exciton lifetime using formula:

$$\gamma(0) = \frac{2\pi e^2 \Omega(0)^2}{\hbar c^2} \frac{\mu^2_{V_{\text{cell}}}}{V_{\text{cell}}} \tag{2}$$

$\frac{\mu^2_{V_{\text{cell}}}}{V_{\text{cell}}}$ is the squared exciton transition dipole matrix element per unit cell and $\Omega(0)$ is the excitation energy of a zero-momentum exciton, respectively. Theses parameters are calculated from the BSE calculations:

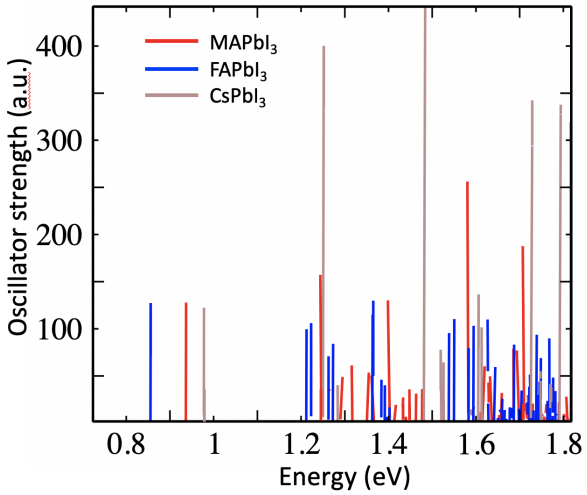

Figure S15: Oscillator strength for $MAPbI_3$, $FAPbI_3$, and $CsPbI_3$, respectively.

TABLE IX: Table VI. Exciton lifetime computed using mBSE approach

$APbX_3$	$\Omega(0)$ (eV)	$\frac{\mu^2_{V_{\text{cell}}}}{V_{\text{cell}}}$ (a.u.)	lifetime (ps)
$MAPbI_3$	0.94	127.8	1.91
$FAPbI_3$	0.86	127.4	2.29
$CsPbI_3$	0.99	117	1.87

TABLE X: Comparison between exciton lifetime computed using Wannier Mott and mBSE approach

$APbX_3$	Wannier-mott (ps)	model-BSE (ps)
$MAPbI_3$	13.77	1.91
$FAPbI_3$	19.85	2.29
$CsPbI_3$	12.51	1.87

From Table X, both the approaches result in exciton lifetime in order of ps range. Note that by taking momentum dependence and dark states into account, an effective radiative lifetime τ_{eff}, can be increased to an order of ns.

XIX. Direct-indirect nature of the bandgap (Rashba splitting)

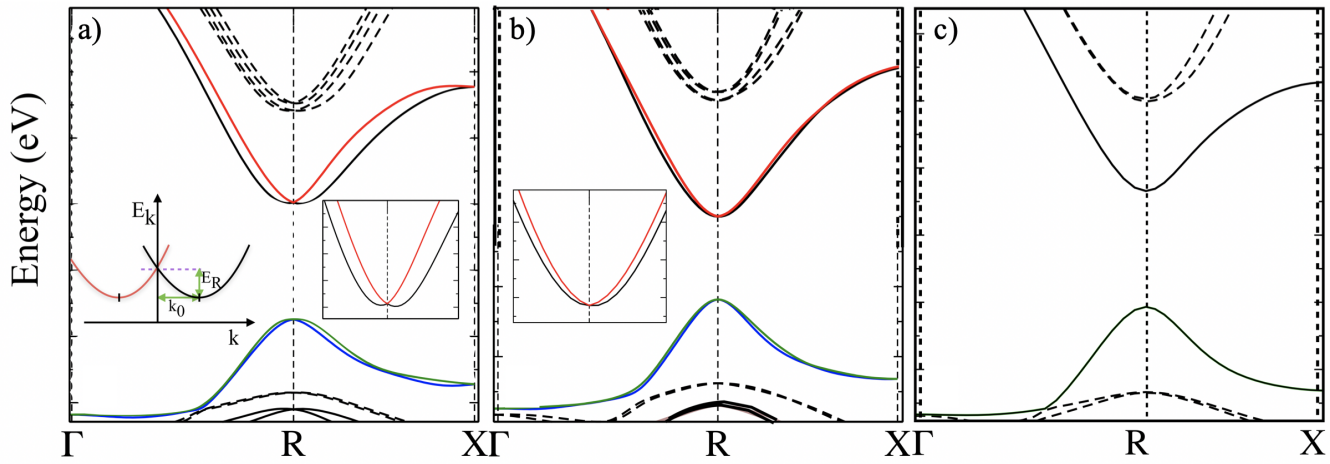

Figure S16: The Rashba-Dresselhaus splitting of the CBM in the R → X and R → Γ directions for (a) $MAPbI_3$ (b) $FAPbI_3$ and (c) $CsPbI_3$. (a) and (b) show inset of zoomed section of the split conduction bands. The spin split valence bands are shown in green and blue solid lines. The conduction bands are denoted by black and red solid lines. The other bands are shown by dashed black lines.

The splitting of bands due to SOC and lack of inversion symmetry result in the Rashba splitting of bands. Note that, for $APbX_3$ perovskites, the Rashba effect is a bit controversial topic because this system intrinsically does not have broken inversion symmetry. There are some dipole fluctuations and disorders which may give some Rashba splitting. The Rashba effect is dominant near the CBm, because of the strong influence of SOC towards heavier atom Pb (main contributor at the CBm). The vertical energy difference (E_R) between slightly shifted CBm and the conduction band energy at R, leads to indirect nature of the bandgap (see inset of Fig S16(a)). The values of E_R for $MAPbI_3$ along R → X and R → Γ directions are 22 meV in agreement with literature [29] and 12.8 meV, respectively. However, for $FAPbI_3$, the calculated values are 0.59 meV (R → X) and 2 meV (R → Γ), respectively. Notably, due to slight change from direct to indirect (in meV), the absorption spectrum is hardly affected by the presence of an indirect gap. The direct-indirect nature of the bandgap allows photogenerated charge carriers to relax into indirect band, whereas direct bandgap allows strong absorption of light. The indirect bandgap may reduce the possibility of radiative recombination of e-h, on the contrary, which is active in direct bandgap semiconductors.
The strength of the Rashba effect can be obtained by the parameter $a = 2E_R/k$, where E_R is the amplitude of the band splitting in a R → X and R → Γ directions [30] (see the inset of Fig S16(a)). For $MAPbI_3$, the estimated a values in the R → X and R → Γ directions are 1.96 eVÅ and 1.01 eVÅ, respectively. For $FAPbI_3$, a values in the R → X and R → Γ directions are 0.17 eVÅ and 0.77 eVÅ, respectively. Hence, $MAPbI_3$ and $FAPbI_3$, have significant Rashba splitting, which is completely absent in cubic $CsPbI_3$ (see Fig S16). The interplay of a low recombination rate (due to indirect gap) and strong absorption (direct gap) indicate the high solar efficiencies of HIOPs.

XX. Effective dielectric constant

The Eq. 5 as mentioned in the main manuscript is:

$$\varepsilon_{\text{eff}}^{-1} = 1 + \frac{2}{\pi}\int_0^{\infty} \frac{\text{Im}(\varepsilon^{-1}(\omega))}{\omega + E_B} \tag{3}$$

Here, $\varepsilon_{\text{eff}}^{-1}$ is the wave vector dependent effective inverse dielectric function and $\varepsilon(\omega)$ is screening due to phonons. The term $-\text{Im}(\varepsilon^{-1}(\omega))$ describes the energy loss function that is calculated from the real and imaginary part of the dielectric function. This equation gives ε_{eff} as a function of exciton binding energy (E_B) i.e $\varepsilon_{\text{eff}}(E_B)$.

The Bethe-Salpeter Equation (BSE) for excitons with zero centre of mass momentum $|S\rangle = \sum_{v'c'k'} A^S_{vck}|vck\rangle$:

$$\left(E^{QP}_{ck} - E^{QP}_{vk}\right) A^S_{vck} + \sum_{v'c'k'} \left\langle vck \left| K^{eh}\left(\Omega^S\right)\right| v'c'k'\right\rangle A^S_{v'c'k'} = \Omega^S A^S_{vck} \tag{4}$$

where A^S_{vck} and Ω^S are the quasielectron-quasihole (e-h) coupling coefficients and exciton energy, respectively. The e-h interaction kernel comprises the "direct" and "exchange" terms, i.e $K^{eh}\left(\Omega^S\right) = -K^{\mathrm{eh}}\left(\Omega^S\right) + K^{\mathrm{exch}}$. The attractive direct term dominates by far and describes the e-h interaction via an effective screened Coulomb interaction $\tilde{W} \equiv \tilde{\varepsilon}^{-1}v$. The expression for the effective dielectric function $\tilde{\varepsilon}^{-1}$ is quite complex as it reflects the fact that an electron excited into a conduction band probes the density response of the system with a hole in the valence bands.
The effective dielectric function incorporates dynamical effects and can be written by neglecting quasiparticle and exciton lifetime effects due to electron-electron interactions:

$$\begin{aligned}\tilde{\varepsilon}^{-1}_{GG'_{cv,k+q};c'v',k}\left(q;\Omega^S\right) = \delta_{GG'} - \tfrac{1}{\pi}P\int_0^\infty d\omega Im\varepsilon^{-1}_{GG'}(q,\omega)\\ \times\left\{\frac{1}{\Omega^S-\omega-\left(E^{\mathrm{QP}}_{ck+q}-\mathrm{E}^{\mathrm{QP}}_{v'k}\right)}+\frac{1}{\Omega^{\mathrm{S}}-\omega-\left(E^{\mathrm{QP}}_{c'k}-\mathrm{E}^{\mathrm{QP}}_{\mathrm{vk}+q}\right)}\right\}\end{aligned} \tag{5}$$

Using the Kramers-Kronig relations obeyed by ε^{-1}, one can write

$$\begin{aligned}\tilde{\varepsilon}^{-1}_{\mathbf{GG}_{\mathrm{cv},k+q;c'v',k}}\left(q;\Omega^S\right) = \varepsilon^{-1}_{\mathbf{GG}'}(q,0) - \frac{1}{\pi}P\int_0^\infty d\omega\,\mathrm{Im}\,\varepsilon^{-1}_{\mathbf{GG}'}(q,\omega)\\ \times\left\{\frac{2}{\omega}+\frac{1}{\Omega^S-\omega-\left(E^{\mathrm{QP}}_{ck+q}-\mathrm{E}^{\mathrm{QP}}_{v'k}\right)}+\frac{1}{\Omega^{\mathrm{S}}-\omega-\left(E^{\mathrm{QP}}_{c'k}-\mathrm{E}^{\mathrm{QP}}_{\mathrm{vk}+q}\right)}\right\}\end{aligned} \tag{6}$$

The static approximation is obtained by setting $E^{QP}_{ck} - E^{QP}_{v'k+q} \approx E^{QP}_{c'k+q} - E^{QP}_{vk} \approx \Omega^S$. First order corrections in dynamical effects can be obtained by considering the case of a bound exciton with most of the contributing e-h pairs localized near the onset of the e-h continuum. A better approximation is to assume $E^{QP}_{ck} - E^{QP}_{v'k+q} \approx E^{QP}_{c'k+q} - E^{QP}_{vk} \approx E^{cont}_S$. Then Eq. 3 reduces to:

$$\begin{aligned}\tilde{\varepsilon}^{-1}_{\mathbf{GG}_{\mathrm{cv},k+q;c'v',k}}\left(q;\Omega^S\right) \approx &\varepsilon^{-1}_{\mathbf{GG}'}(q,0) - \frac{2}{\pi}\\ &\times\int_0^\infty d\omega Im\varepsilon^{-1}_{\mathbf{GG}'}(q,\omega)\left\{\frac{1}{\omega}-\frac{1}{\omega+\mathrm{E_B}}\right\}\end{aligned} \tag{7}$$

The detailed analysis of the above equations can be found in the following references [31, 32].

[1] C. Quarti, E. Mosconi, J. M. Ball, V. D'Innocenzo, C. Tao, S. Pathak, H. J. Snaith, A. Petrozza, and F. De Angelis, Energy & Environmental Science **9**, 155 (2016).
[2] A. Kojima, K. Teshima, Y. Shirai, and T. Miyasaka, Journal of the American Chemical Society **131**, 6050 (2009).
[3] F. Zhang, J. F. Castaneda, S. Chen, W. Wu, M. J. DiNezza, M. Lassise, W. Nie, A. Mohite, Y. Liu, S. Liu, et al., arXiv preprint arXiv:1907.03434 (2019).
[4] J. Qiu, Y. Qiu, K. Yan, M. Zhong, C. Mu, H. Yan, and S. Yang, Nanoscale **5**, 3245 (2013).
[5] M. Jain, A. Singh, P. Basera, M. Kumar, and S. Bhattacharya, Journal of Materials Chemistry C (2020).
[6] E. Mosconi, P. Umari, and F. De Angelis, Physical Chemistry Chemical Physics **18**, 27158 (2016).
[7] P. Basera, S. Saini, E. Arora, A. Singh, M. Kumar, and S. Bhattacharya, Scientific reports **9**, 1 (2019).
[8] P. Basera, M. Kumar, S. Saini, and S. Bhattacharya, Physical Review B **101**, 054108 (2020).
[9] D. Demchenko, N. Izyumskaya, M. Feneberg, V. Avrutin, Ü. Özgür, R. Goldhahn, and H. Morkoç, Physical Review B **94**, 075206 (2016).
[10] J.-W. Lee, D.-J. Seol, A.-N. Cho, and N.-G. Park, Advanced Materials **26**, 4991 (2014).
[11] S. Aharon, A. Dymshits, A. Rotem, and L. Etgar, Journal of Materials Chemistry A **3**, 9171 (2015).
[12] S. Pang, H. Hu, J. Zhang, S. Lv, Y. Yu, F. Wei, T. Qin, H. Xu, Z. Liu, and G. Cui, Chemistry of Materials **26**, 1485 (2014).
[13] G. E. Eperon, G. M. Paterno, R. J. Sutton, A. Zampetti, A. A. Haghighirad, F. Cacialli, and H. J. Snaith, Journal of Materials Chemistry A **3**, 19688 (2015).
[14] Z. Yang, A. Surrente, K. Galkowski, A. Miyata, O. Portugall, R. Sutton, A. Haghighirad, H. Snaith, D. Maude, and P. Plochocka, ACS Energy Letters **2**, 1621 (2017).
[15] L. Leppert, T. Rangel, and J. B. Neaton, Physical Review Materials **3**, 103803 (2019).
[16] M. R. Filip, C. Verdi, and F. Giustino, The Journal of Physical Chemistry C **119**, 25209 (2015).
[17] A. Miyata, A. Mitioglu, P. Plochocka, O. Portugall, J. T.-W. Wang, S. D. Stranks, H. J. Snaith, and R. J. Nicholas, Nature Physics **11**, 582 (2015).

[18] K. Galkowski, A. Mitioglu, A. Miyata, P. Plochocka, O. Portugall, G. E. Eperon, J. T.-W. Wang, T. Stergiopoulos, S. D. Stranks, H. J. Snaith, et al., Energy & Environmental Science **9**, 962 (2016).
[19] P. Umari, E. Mosconi, and F. De Angelis, The journal of physical chemistry letters **9**, 620 (2018).
[20] M. Bokdam, T. Sander, A. Stroppa, S. Picozzi, D. Sarma, C. Franchini, and G. Kresse, Scientific reports **6**, 1 (2016).
[21] Z. Yang, A. Surrente, K. Galkowski, N. Bruyant, D. K. Maude, A. A. Haghighirad, H. J. Snaith, P. Plochocka, and R. J. Nicholas, The journal of physical chemistry letters **8**, 1851 (2017).
[22] A. Amat, E. Mosconi, E. Ronca, C. Quarti, P. Umari, M. K. Nazeeruddin, M. Gra tzel, and F. De Angelis, Nano letters **14**, 3608 (2014).
[23] U.-G. Jong, C.-J. Yu, Y.-S. Kim, Y.-H. Kye, and C.-H. Kim, Physical Review B **98**, 125116 (2018).
[24] M. Afsari, A. Boochani, and M. Hantezadeh, Optik **127**, 11433 (2016).
[25] L. G. Ferreira, M. Marques, and L. K. Teles, Physical Review B **78**, 125116 (2008).
[26] W. Chen and A. Pasquarello, Physical Review B **90**, 165133 (2014).
[27] C. D. Spataru, S. Ismail-Beigi, R. B. Capaz, and S. G. Louie, Physical review letters **95**, 247402 (2005).
[28] L. Hu, C. Xu, L. Peng, F. L. Gu, and W. Yang, Journal of Materials Chemistry A **6**, 15027 (2018).
[29] C. Motta, F. El-Mellouhi, S. Kais, N. Tabet, F. Alharbi, and S. Sanvito, Nature communications **6**, 7026 (2015).
[30] S. Hu, H. Gao, Y. Qi, Y. Tao, Y. Li, J. R. Reimers, M. Bokdam, C. Franchini, D. Di Sante, A. Stroppa, et al., The Journal of Physical Chemistry C **121**, 23045 (2017).
[31] C. D. Spataru and F. Léonard, Chemical Physics **413**, 81 (2013).
[32] G. Strinati, La Rivista del Nuovo Cimento (1978-1999) **11**, 1 (1988).